

Transition in high velocity ratio coaxial jets analysed from direct numerical simulations

Carlos B da Silva¹, Guillaume Balarac and Olivier Métais²

Equipe MoST/LEGI/Institut de Mécanique de Grenoble, BP 53,
38041 Grenoble Cedex 09, France
E-mail: olivier.metais@hmg.inpg.fr

Received 25 April 2003
Published 8 July 2003

Abstract. Direct numerical simulations are performed to analyse the instability, transition scenario and resulting topology from high velocity ratio coaxial jets ($r_u = 3.3$ and 23.5). The inner and outer shear layers roll up into axisymmetric vortex rings due to the Kelvin–Helmholtz instability. For $r_u = 3.3$ the outer primary vortices evolve according to the theory considering an isolated mixing layer profile, and impose their evolution upon the inner structures which are ‘locked’ into the outer ones. For $r_u = 23.5$ there is a big recirculation region that does not affect the development of the Kelvin–Helmholtz instabilities. The preferred mode for simple (non-coaxial) round jets is well recovered at the end of the potential core region in the case $r_u = 3.3$ but not when $r_u = 23.5$ due to the presence of the backflow region. The structure of the preferred mode is the same in both cases, however, and consists in a helical arrangement ($m = 1$). Finally, when the bubble is present one can see that the inner streamwise structures, corresponding to the secondary instabilities, are stretched by the presence of the bubble which acts as an additional source of axial vorticity production.

PACS numbers: 47.27.Wg, 47.27.Eq, 47.27.Cn

¹ Present address: Instituto Superior Técnico, LASEF, Dep. Eng. Mecânica, Pav. Mecânica 1, 1: andar, Av. Rovisco Pais, 1049-001 Lisboa, Portugal.

² Author to whom any correspondence should be addressed.

Contents

1	Introduction	2
2	Numerical method	4
3	Direct numerical simulations of coaxial jets	4
4	Results and discussion	6
4.1	Global flow picture	6
4.1.1	Visualizations.	6
4.1.2	Statistics.	8
4.2	Instabilities and transition	12
4.2.1	Primary instabilities: jet shear layer mode.	12
4.2.2	Primary instabilities: jet preferred mode.	14
4.2.3	Secondary instabilities.	16
5	Conclusions	17
	Acknowledgment	17
	References	18

1. Introduction

Coaxial jet flows are often used in industrial applications as an effective way of mixing two different fluid streams (e.g. mixing air and combustible in jet engines). A coaxial jet is made when a fluid stream with velocity U_2 , issuing from an outer annulus of diameter D_2 , is added into a round jet flow with velocity U_1 , and (inner) nozzle diameter D_1 ($D_1 < D_2$). Annular jets correspond to the case when there is no inner fluid stream, $U_1 = 0$.

It is well known that small scale mixing is mainly governed by the small scale turbulence level, whereas large scale mixing is controlled by the large scale coherent structures. It is therefore very important to understand the detailed dynamics of these structures, even in simpler flow configurations (i.e. constant density and low Reynolds numbers). In this context, several authors analysed the impact of the global flow parameters in the subsequent topology of coaxial jets [1, 2].

The existence of two (inner and outer) shear layer regions was evidenced by Ko and Kwan [3] and Kwan and Ko [4] in coaxial jets, through the observation of two different peak spectrum frequencies corresponding to the passing frequencies of vortices originated in the inner and outer shear layers. They also noticed the formation of two potential cores, corresponding to each of these regions. In their case ($U_2 < U_1$ and U_2 relatively small) the outer stream acts mainly as a coflowing velocity which does not modify substantially the inner jet dynamics. Djeridane [5] analysed the effect of superimposing a small co-flow into a round jet and concluded that for co-flowing velocities smaller than 10% of the jet velocity the co-flow has only a minor influence on the spatial jet evolution.

Dahm *et al* [1] highlighted the importance of the initial outer to inner velocity ratio $r_u = U_2/U_1$, in the selection of the several existing flow regimes. For low initial velocity ratios ($0.59 < r_u < 0.71$) the outer shear layer instability rolls up into axisymmetric vortex rings ($m = 0$) that turn further downstream into a helical shaped structure ($m = 1$), in agreement with the linear stability theory results for a single-jet flow. These primary rings travel downstream at a frequency which agrees well with the value predicted by the linear instability theory considering

an initial ‘wake + mixing layer’ velocity profile. The inner shear layer, on the other hand, has a lethargic behaviour and never rolls up into vortical structures before being dominated by the helical vortices from the outer layer. But for large initial velocity ratios ($r_u = 2.56$) the inner shear layer also develops into ring shaped vortices which interact with the outer vortex structures. One of the most important results from this study was the observation of a ‘locking’ phenomenon between the two shear layers. It was observed that the vortex passage frequency from the inner shear layer differs from the value predicted by the stability analysis of a single shear layer with the same characteristics. The reason for this comes from the fact that the vortices from the inner shear layer are trapped into the free spaces left between two consecutive outer layer vortices. The latter modify the ‘normal’ inner shear layer development which is in this way ‘locked’ into the outer layer dynamics. Another important observation is related to the initial vorticity thickness of the inner and outer shear layers. For the same initial velocity ratio ($r_u = 1.0$), but using different absolute velocities, a dramatically different flow topology could be observed, due to the difference in the initial shear layer momentum thicknesses. In general, smaller initial vorticity thicknesses lead to a faster roll-up process (for the same velocity jump), thus causing very different flow topologies.

The influence of the velocity ratio r_u in the flow regimes of coaxial jets was also analysed by Rehab *et al* [2]. They considered only $r_u > 1$ cases and found the existence of a critical velocity ratio r_{uc} above which the flow develops a big reverse flow region. The value of r_{uc} depends on the shape of the inlet velocity profiles (nozzle shape) and varies in the range of about $5 < r_{uc} < 8$. A big recirculation bubble is always present in annular jets, which can be viewed as coaxial jets with $r_u = U_2/U_1 = \infty$ [6]. For smaller than critical velocity ratios ($1 < r_u < r_{uc}$) the structures from the fast stream ‘pinch’ the central jet at the end of the potential core x_{1p} . The pinching frequency is equal to the outer jet mode, $fD_2/U_2 \approx 0.4$. The value of x_{1p} decreases with increasing r_u . For greater than critical velocity ratios ($r_u > r_{uc}$) a large recirculating bubble forms with a size of the order of the inner diameter D_1 , which grows with increasing velocity ratio, r_u . One of the more interesting features of this backflow region is the fact that it oscillates and rotates with the same frequency in a pure precession mode. This frequency is fixed by D_1 and U_2 and is one order of magnitude smaller than the original Kelvin–Helmholtz instability mode. Finally, Rehab [7] also analysed the influence of the inlet nozzle geometry in the flow regimes of coaxial jets. An important parameter for this study is the ratio of outer to inner nozzle diameters $\beta = D_2/D_1$. It was observed that an increase in the value of β causes an increase in both the inner potential core x_{1p} and in the critical velocity ratio r_{uc} .

Numerical studies of coaxial jets are very rare and are often restricted to 2D cases, due to the need for massive computer resources. Among the limited number of numerical works on coaxial jets are the works of Akselvoll and Moin [8] who studied coannular jets by large-eddy simulations in a fully developed turbulent configuration. Salvetti [9] made direct numerical simulations (DNSs) of axisymmetric (2D) coaxial jets to analyse the effects of the inlet condition on the dynamics of the vortical structures. Salvetti [10] also studied numerically the effect of inner/outer mutual interactions. It was observed that vortical inner/outer interactions tend to increase with increasing velocity ratio r_u . Finally, da Silva and Métais [11] carried out what is maybe the first DNS of a coaxial jet, in order to study the flow topology in an excited (*varicose*) configuration.

The present work uses DNS to analyse the instability, transition scenario and resulting topology from high velocity ratio coaxial jets. DNSs are restricted to low Reynolds numbers but a correct understanding of the flow topology at low Reynolds numbers or in transition regions can be useful to understand the dynamics of high Reynolds number cases since, as in single-jet flows, there are still ‘vestiges’ of some ‘coherence’ caused mainly by vortex related features that persist even in high Reynolds numbers (e.g. the preferred mode in single-jet flows).

This article is organized as follows. The next section 2 describes the governing equations and numerical methods. Section 3 details the physical and computational parameters of the various calculations. The results obtained from DNSs of coaxial jets are analysed and discussed in section 4. Section 5 reviews the main results and conclusions.

2. Numerical method

All the simulations presented here were performed with a code that solves the full, three-dimensional, incompressible Navier–Stokes equations. The code is a finite difference solver that uses both sixth order ‘compact’ [12] and pseudo-spectral [13] schemes for spatial discretization. Pressure–velocity coupling is assured by a fractional step method [14], requiring the resolution of a Poisson equation to insure incompressibility of the velocity field. A three-step, third order Runge–Kutta scheme [15] is used for temporal discretization. As inlet boundary condition, each time step a given velocity profile is prescribed at the inlet, the details of which will be given in the next section. The outlet boundary condition is of non-reflective type [16].

This code was developed by Gonze [17] and was intensively validated both in round and plane jet configurations [18, 19]. Full numerical discretization details can be found in [20].

The code was parallelized using the PVM library and the calculations were carried out on a ten-node Linux Beowulf cluster. Details can be found in [21].

3. Direct numerical simulations of coaxial jets

Two DNSs were carried out (DNS1, DNS2). In both cases the shape of the inlet velocity profile is

$$\vec{U}(\vec{x}_0, t) = \vec{U}_{med}(\vec{x}_0) + \vec{U}_{noise}(\vec{x}_0, t), \quad (1)$$

where $\vec{U}(\vec{x}_0, t)$ is the instantaneous inlet velocity vector, which is prescribed as inlet condition, for each time step. In equation (1) $\vec{U} = (U, V, W)$, where U, V and W are the streamwise, normal and spanwise velocities, respectively. We will also use the cylindrical coordinates $\vec{U} = (u_x, u_r, u_\theta)$, where u_x, u_r and u_θ represent the axial, radial and tangential velocity components, respectively.

One of the main difficulties in the numerical simulation of coaxial jets results from the complexity of the inlet velocity profile which has to be accurately represented. As stressed by Dahm *et al* [1], each one of the two shear layers can be described as a combined ‘wake + mixing layer’ profile. But, as shown by Rehab *et al* [2], the ‘wake’ part of the mean streamwise velocity profiles disappears very fast. In the experimental measurements by Rehab *et al* [2] one can notice that the whole ‘wake’ part of the velocity profile disappears long before $x/D_1 = 1$. Therefore, it seems that an inlet velocity profile made up of two ‘hyperbolic tangent’ velocity profiles could be a good approximation to the ‘real’ velocity profile. In addition to this, this makes possible a rigorous definition of the governing global parameters.

Figure 1 shows a sketch of a typical idealized inlet velocity profile. Each velocity jump is represented by a typical mixing layer (hyperbolic tangent) velocity profile. This was the methodology adopted in the present study. The mean velocity profile is therefore represented as

$$U_{med}(\vec{x}_0) = \begin{cases} \frac{U_1 + U_2}{2} + \frac{U_1 - U_2}{2} \tanh\left(\frac{r - R_1}{2\theta_{01}}\right) & \text{for } r < R_m \\ \frac{U_2 + U_3}{2} + \frac{U_2 - U_3}{2} \tanh\left(\frac{r - R_2}{2\theta_{02}}\right) & \text{for } r > R_m. \end{cases}$$

Here U_1 is the inner coaxial jet velocity, U_2 is the outer velocity and U_3 is a very small co-flow. R_1, R_2 and $R_m = (R_1 + R_2)/2$ are the inner, outer and mean radii, and θ_{01} and θ_{02} are the initial

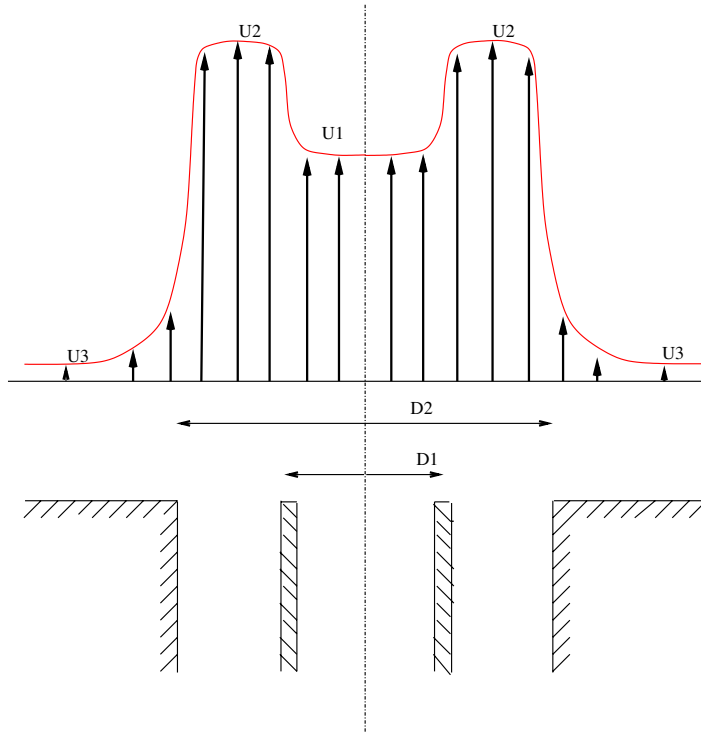


Figure 1. Sketch of the inlet velocity profile. U_1 is the inner jet velocity coming out of a nozzle with a diameter D_1 . U_2 is the velocity of the outer jet stream, issuing from a diameter $D_2 > D_1$. θ_1 and θ_2 are the momentum thicknesses from the inner shear layer (velocity jump from U_1 to U_2) and outer shear layer (velocity jump from U_1 to U_2), respectively.

momentum thicknesses from the inner and outer shear layers, respectively. For each station x , the inner and outer momentum thicknesses are defined by

$$\theta_1(x) = \int_0^{R_m} \left[\frac{u_x(x, r) - u_{min}(x)}{u_{max}(x) - u_{min}(x)} \right] \left[1 - \frac{u_x(x, r) - u_{min}(x)}{u_{max}(x) - u_{min}(x)} \right] dr \quad (2)$$

$$\theta_2(x) = \int_{R_m}^{\infty} \left[\frac{u_x(x, r) - u_{min}(x)}{u_{max}(x) - u_{min}(x)} \right] \left[1 - \frac{u_x(x, r) - u_{min}(x)}{u_{max}(x) - u_{min}(x)} \right] dr \quad (3)$$

where $u_{max}(x)$ and $u_{min}(x)$ are the maximum and minimum velocities from the inner or outer shear layers.

Notice that the mean normal and spanwise velocities were set to zero at the inlet

$$V_{med}(\vec{x}_0) = W_{med}(\vec{x}_0) = 0. \quad (4)$$

$\vec{U}_{noise}(\vec{x}_0, t)$ is the inlet noise profile which is given by

$$\vec{U}_{noise}(\vec{x}_0, t) = A_n U_{base}(\vec{x}_0) \vec{f}^T. \quad (5)$$

A_n is the maximum amplitude of the incoming noise and $U_{base}(\vec{x}_0)$ is a function that sets the noise location mainly in the shear layer gradients:

$$U_{base}(\vec{x}_0, r) = \begin{cases} 0.5 & \text{if } 0.85 > r/R_1 \\ 1.0 & \text{if } 0.85 < r/R_1 < 1.15 \\ 1.0 & \text{if } 0.85 < r/R_2 < 1.15 \\ 0 & \text{otherwise.} \end{cases}$$

\vec{f}' is a random noise designed to satisfy a given energy spectrum

$$E(k) \propto k^s \exp\left[-\frac{s}{2}(k/k_0)^2\right]. \quad (6)$$

$k = (k_y^2 + k_z^2)^{1/2}$ is the wavenumber norm in the (y, z) plane. The exponent s , and peak wavenumber k_0 , were chosen to have an energy input at small scales (high k_0) and a large-scale spectral behaviour typical of decaying isotropic turbulence ($s \leq 4$). Note that the random noise is imposed on the three velocity components.

Both simulations were carried out on the same grid which consists in $231 \times 256 \times 256$ points and allows a domain size of $10.8D_1 \times 7.1D_1 \times 7.1D_1$, along the streamwise (x) and the two transverse directions (y, z), respectively. The mesh size is uniform in all three directions. In both simulations the Reynolds number and the ratio of outer to inner diameters was $Re_{D_1} = \frac{U_2 D_1}{\nu} = 3000$ and $\beta = \frac{D_2}{D_1} = 2$, respectively. The ratio of the jet radius to the initial shear layer momentum thicknesses was $\frac{R_1}{\theta_{01}} = \frac{R_2}{\theta_{02}} = 13$ and the maximum noise amplitude was limited to $A_n = 4.0\%$.

The difference between the two simulations concerns the initial velocity ratio $r_u = U_2/U_1$. In the first simulation (DNS1), this ratio was set to $r_u = U_2/U_1 = 3.3$. The second simulation (DNS2) uses $r_u = U_2/U_1 = 23.5$. The co-flow was such that $U_3/U_2 = 0.04$, for both simulations. The co-flow is then very small, and does not influence the jet dynamics [5, 20].

4. Results and discussion

This section analyses the results from simulations DNS1 and DNS2. We start looking into the global picture of the flow, mainly through visualization of instantaneous quantities. After that, the details of the transition process in coaxial jets will be analysed.

4.1. Global flow picture

4.1.1. Visualizations. One can form a first picture of the whole coaxial jet flow from simulations DNS1 and DNS2 by looking at figures 2(a) and (b). The figures show instantaneous fields of positive Q [22, 23] coloured by the azimuthal vorticity, Ω_θ

$$\Omega_\theta = \left(\frac{\partial u_r}{\partial x} - \frac{\partial u_x}{\partial r} \right). \quad (7)$$

Blue/red corresponds to positive/negative values of Ω_θ , respectively. The main features of both flows can be appreciated here. In the early transition stages ($x/D_1 < 2$), both the inner/outer shear layers roll up into vortex rings. Since the Q isosurfaces are coloured by Ω_θ the fact that the inner/outer rings appear in blue and red shows that the vortices turn in opposite sense. These structures appear in both simulations, and at each shear layer (inner/outer) and are an expected consequence of the Kelvin–Helmholtz instability created by the shape of the initial velocity profiles. Notice that the rings seem to preserve the same wavelength spacing λ_0 , until $x/D_1 \approx 7$ where they begin to disappear, ‘swallowed’ by the growth of small scale turbulence. Around the middle of the computational domain $x/D_1 \approx 7$, pairs of streamwise vortices appear between two consecutive outer rings, in agreement with the classical scenario of transition in free

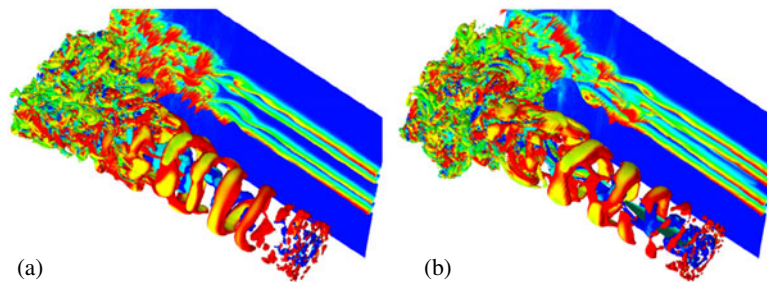


Figure 2. Isosurfaces of positive Q , coloured by the azimuthal vorticity, Ω_θ in DNS1 (see animation) (a) and DNS2 (see animation) (b). Blue/red stands for positive/negative values of Ω_θ , respectively.

shear layers. Further downstream, just before the end of the computational domain, the growth of small scale turbulence near the structures as well as their breakdown makes their identification very difficult. By $x/D_1 \approx 8$ the structures no longer exhibit any preferential direction and seem ‘isotropic’. This is an indication that the flow is quickly reaching a state of fully developed turbulence.

We continue the flow characterization with figures 3(a) and (b) showing contours of streamwise velocity for both simulations. The streamwise velocity contours remain smooth until $x/D_1 \approx 5$, in both simulations. The most important observation from this figure, however, is the existence of a strong back-flow region in DNS2 which can be seen through blue contours of $u_x(x, r)$, corresponding to a region of $u_x(x, r) < 0$. The recirculation bubble is centred at $x/D_1 \approx 2.5$ (see figure 3(b)). Similar back-flow regions were observed in experimental studies of coaxial jets with high velocity ratios [2] and are always present in co-annular jets [6], where no inner jet exists and therefore can be seen as a coaxial jet with velocity ratio $r_u = U_2/U_1 = \infty$. Notice that around this location the flow evolves smoothly, therefore indicating that the recirculation bubble is either stationary or evolving slowly, since it seems to be surrounded by laminar flow. It is also interesting to note the downstream evolution of the two outer shear layers (i.e. the two layers of maximum streamwise velocity, starting at $r/D_1 = 0.5$). Whereas in DNS1 (no recirculation bubble) the outer shear layer thickness grows as the flow evolves downstream, in DNS2 the two outer streams converge after the back-flow region, leading to a decrease in the overall shear layer thickness at $x/D_1 \approx 7$ (see figure 5(e)).

Next (figures 4(a) and (b)) give some insight into the vortical structures of the flow. Again, one sees that the initial evolution of the (inner/outer) shear layers is very smooth. This shows that the present ‘synthetic’ noise used at the inflow boundary allows the flow to evolve ‘naturally’ and to ‘choose’ its primary instabilities from the initial velocity profile characteristics. In DNS1 the first Kelvin–Helmholtz vortices appear at $x/D_1 \approx 5$ both at the outer and inner shear layers. For DNS2, the same structures appear slightly later at $x/D_1 \approx 5.5$ (outer and inner layer). The figures show also what appears to be the occurrence of merging between the primary Kelvin–Helmholtz rollers at $x/D_1 \approx 7$ for the outer shear layers of both flows. The most interesting feature one can observe with these figures is that in each simulation the evolution of the inner and outer layers is not independent. As can be seen in figures 4(a) and (b) after $x/D_1 \approx 5$, the vortices from the inner shear layer are trapped in the free spaces between two consecutive outer layer vortices. This issue will be analysed in detail below. Finally, one can also observe that the outer vortex structures pinch the central jet at $x/D_1 \approx 5$ (for DNS1 and DNS2), in close similarity to the experimental visualizations from [2].

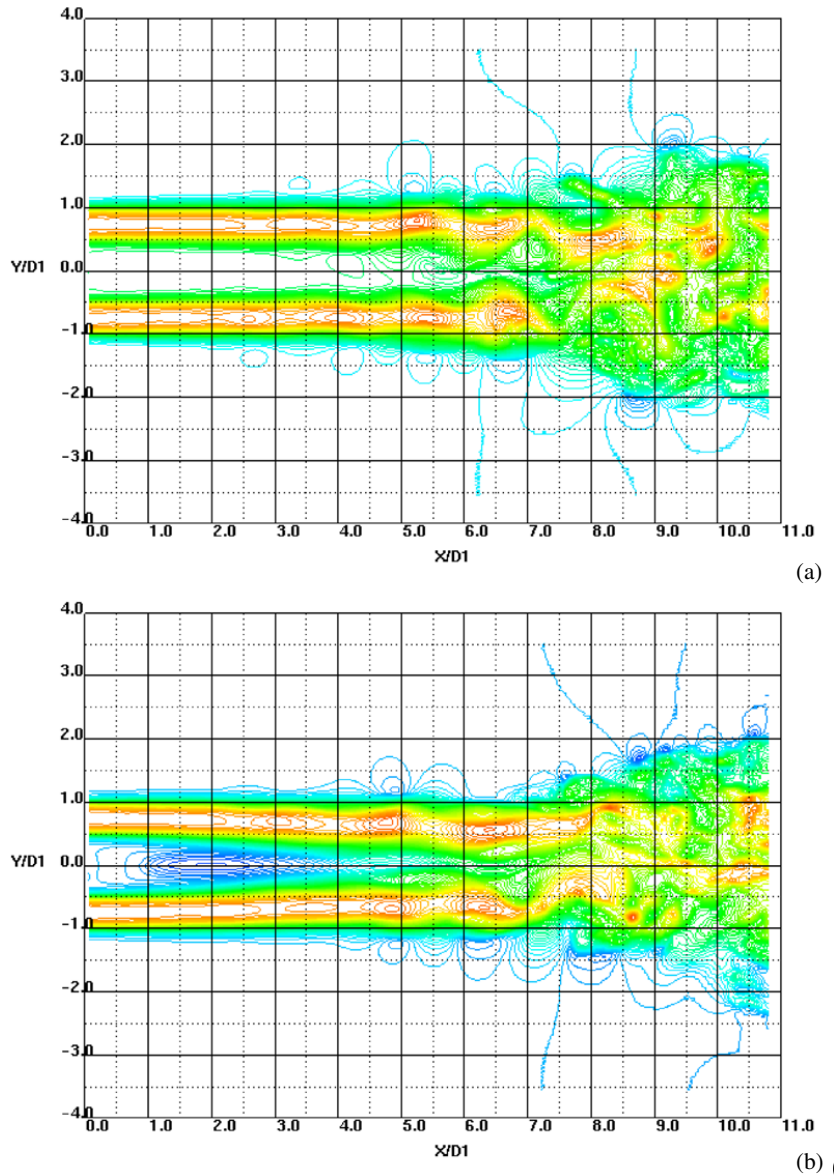


Figure 3. Contours of streamwise velocity $u_x(x, r)$, in DNS1 (a) and DNS2 (b). The contour lines are in a slice which passes through the plane $(x, y, z = 0)$. Negative values of $u_x(x, r)$ are indicated in blue. In simulation DNS2 one can observe a big back-flow region in the first half of the computational domain.

4.1.2. Statistics. To conclude on the flow characterization figures 5(a)–(e) show some one-point statistics for the DNS1 and DNS2 simulations. We use the Reynolds decomposition where an instantaneous field ϕ can be decomposed into $\phi = \langle \phi \rangle + \phi'$, in which $\langle \phi \rangle$ and ϕ' stand for its mean and fluctuating parts, respectively. Here the mean operator $\langle \phi \rangle$, consists in combined space and time averages.

In DNS1 the axial velocity is constant in a region extending to $l_{core}^{in} \approx 5D_1$ at the centreline ($r = 0$) and $l_{core}^{out} \approx 5D_1$ at the centre of the outer jet ($r = R_m$) (figure 5(a)). This shows that in DNS1, two potential core regions exist, one at the inner and another at the outer jet. Similar

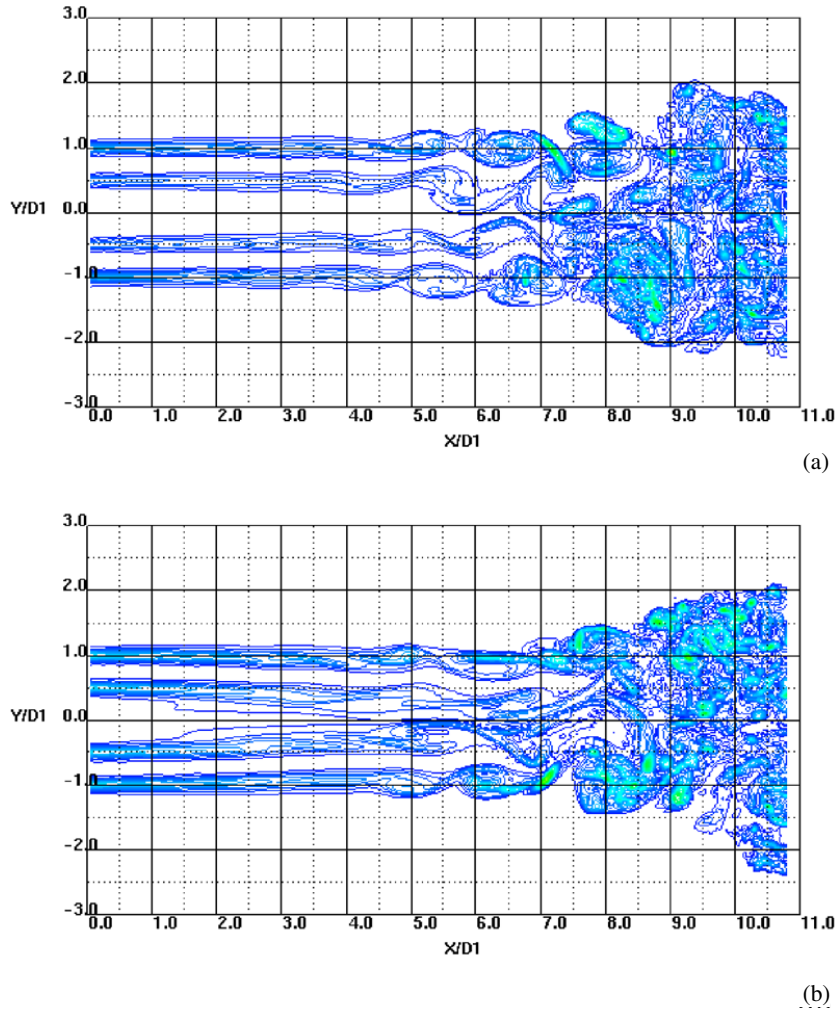


Figure 4. Contours of vorticity modulus $|\vec{\Omega}|$, in DNS1 (a) and DNS2 (b). The contour lines are in a slice which passes through the plane $(x, y, z = 0)$.

coaxial potential cores have been observed experimentally [3, 4]. In DNS2 (see figure 5(b)) the outer jet also exhibits a potential core region, with length $l_{core}^{out} \approx 6D_1$, but the same does not occur in the inner jet. Here the centreline axial velocity is negative between $x/D_1 \approx 0.5$ and $x/D_1 \approx 4.0$, due to the presence of the back-flow region. The axial length of this structure is $l_{bx} \approx 3.5D_1$. Figure 5(b) can also be used to measure the minimum back-flow velocity, and its location. We have $\langle u_x(x, r) \rangle = -3U_1$ at $x/D_1 = 0.75$. The evolution of the axial velocity after the end of each potential core is governed by radial diffusion of linear momentum which transfers momentum from the outer into the inner shear layers. This idea is confirmed in figures 5(c) and (d) showing profiles of axial velocity at several stations for simulations DNS1 and DNS2. Notice that for $x/D_1 = 10$ the velocity profile (for DNS1 and DNS2) has lost its two-layer structure, and the maximum velocity is located at the centreline. Figure 5(d) can help to measure the radial extent of the recirculation bubble: one has roughly, $l_{br} \approx D_1$ at $x/D_1 = 2$.

Finally, figure 5(e) displays the downstream evolution of the shear layer thickness $\delta(x)$ for DNS1 and DNS2, defined as

$$\langle u_x(x, r = \delta(x)) \rangle = \frac{1}{2} (\langle u_x(x, r = r_{max}) \rangle - \langle u_x(x, r = \infty) \rangle), \quad (8)$$

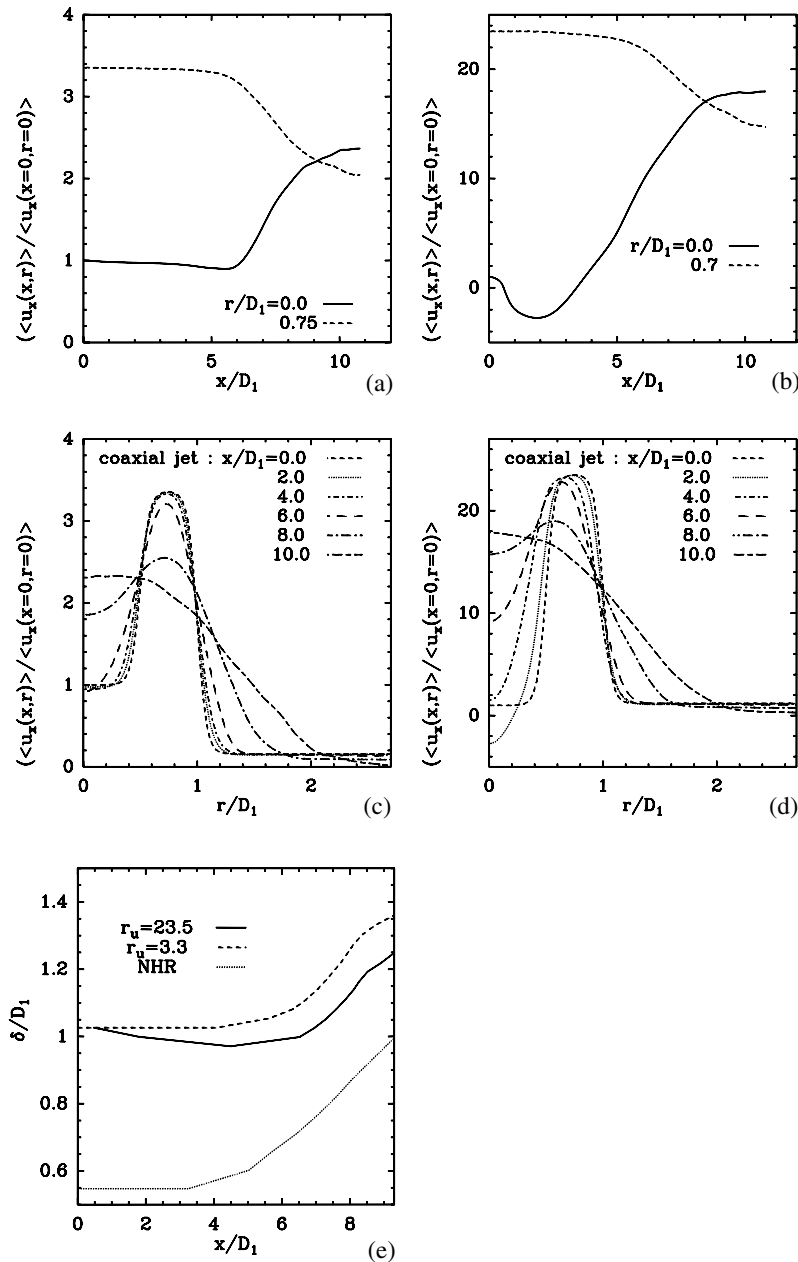


Figure 5. (a) Downstream evolution of the axial velocity component at $r/D_1 = 0$ and $r/D_1 = 0.75$ for DNS1; (b) the same for DNS2; (c) axial velocity profiles for DNS1; (d) the same for DNS2; (e) downstream evolution of the shear layer thickness for DNS1 and DNS2. NHR stands for a round jet at $Re_D = 25\,000$ (from [18]).

where r_{max} is the radial distance at which the axial velocity attains its maximum value, $\max\{\langle u_x(x,r) \rangle\} = \langle u_x(x,r = r_{max}) \rangle$. There is an accentuated difference between the curves in the range $0 < x/D_1 < 7$, where the shear layer thickness for DNS2 decreases. This can be explained by the convergence of the streamlines which tends to follow a recirculation bubble, as already discussed. After $x/D_1 > 7$, however both curves seem to grow with a similar slope and it

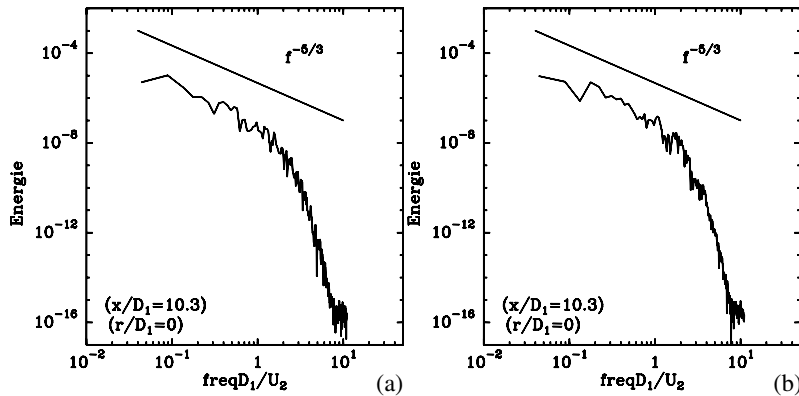


Figure 6. Frequency spectra of the axial velocity signal at $x/D_1 \approx 10$ for DNS1 and DNS2. (a) DNS1; (b) DNS2.

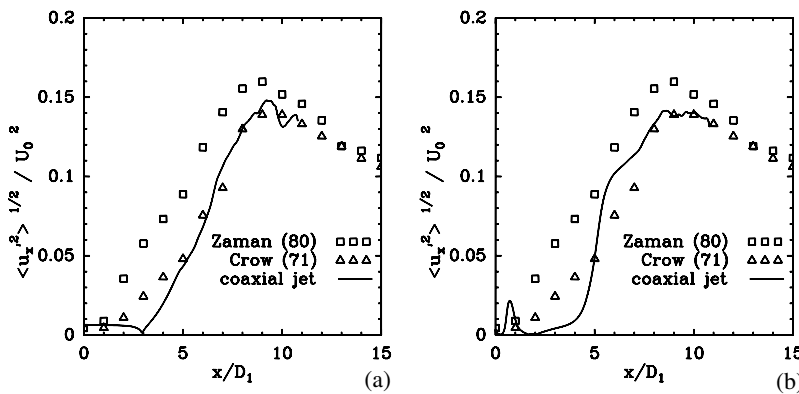


Figure 7. Downstream evolution of the axial normal stresses at the centreline in DNS1 (a) and DNS2 (b), compared with the measurements by Zaman and Hussain [24] and Crow and Champagne [25].

is interesting to note that this slope is the same as found by da Silva and Métais [18] in a round jet (NHR) within the self-similar turbulent regime, at much higher Reynolds number (NHR). In fact, all evidence points to the existence of a fully developed turbulent regime for $x/D_1 = 10$ in both DNS1 and DNS2. To show this, figures 6(a) and (b) show time spectra computed from the axial velocity component at $x/D_1 = 10.3$. The spectra exhibit a $-5/3$ range over about one decade followed by a smooth transition into the dissipative region. This $-5/3$ slope is a good indication that, by that point, the flow has reached a fully developed turbulent state.

Finally, it is also instructive to see the downstream evolution of the axial normal stresses at the centreline in DNS1 and DNS2 (see figure 7). The stresses compare well with the measurements made by Zaman and Hussain [24] and Crow and Champagne [25] in round jets at high Reynolds number. The maximum is roughly the same value ($\langle u^2 \rangle / U_2^2 = 0.14$) and is obtained at the same location ($x/D_1 = 10$), both in the simulations and the experimental data. This peak is followed by a decrease in the stresses at a rate which is also similar in the simulations and experimental data. Note that the difference between DNS1 and DNS2 occurs mainly in the transition region ($x/D_1 < 7$), due to the recirculation bubble. In DNS2 there is a peak in the stresses just before the bubble ($x/D_1 = 0.5$) and a big growth rate just after it ($x/D_1 = 5$). In between, the stresses are smaller than in DNS1 and confirm the visualizations, showing that the

Table 1. Strouhal numbers of the most amplified modes in the outer (o) and inner (i) shear layers for simulations DNS1 and DNS2. The Strouhal number is based on the initial momentum thickness, $Str_{\theta_0} = \frac{f\theta_0}{\Delta U_0}$, where $\Delta U_0 = 0.5(U_{max} + U_{min})$, with U_{max} and U_{min} being the maximum and minimum velocities across each shear layer, respectively. The spectra were computed using time series of the streamwise velocity component located at $(r/D_1, x/D_1) = (1, 3)$ (outer layer) and $(r/D_1, x/D_1) = (0.5, 3)$ (inner layer).

Simulation	Str_{θ}^o	Str_{θ}^i
DNS1	0.028	0.011
DNS2	0.03	0.01

bubble is a quasi-laminar flow. The evolution of the stresses around it can be explained by the high levels of $\partial\langle u \rangle / \partial x$ at those locations, as often occurs near separation regions, which causes high production of axial normal stresses

$$P_{\langle u'^2 \rangle} = - \left[2\langle u'^2 \rangle \frac{\partial \langle u \rangle}{\partial x} + 2\langle u'v' \rangle \frac{\partial \langle u \rangle}{\partial y} + 2\langle u'w' \rangle \frac{\partial \langle u \rangle}{\partial z} \right]. \quad (9)$$

4.2. Instabilities and transition

This section analyses the details of the transition process in DNS1 and DNS2. In particular, the interplay between the inner and outer shear layers is used to account for the particular evolution of the coaxial jet flows.

4.2.1. Primary instabilities: jet shear layer mode. As described before, in the initial stages of transition, the two (inner/outer) shear layers roll up into vortex rings due to the well known Kelvin–Helmholtz instability. The theoretical value of the Strouhal number of the most unstable wave resulting from this instability is [26]

$$Str_{\theta_0} = \frac{f\theta_0}{\Delta U_0} = 0.033, \quad (10)$$

where $\Delta U_0 = 0.5(U_{max} + U_{min})$ and U_{max} and U_{min} are the maximum and minimum velocities across the shear layer, respectively. But we saw also that each shear layer is in some way influenced by the presence of its neighbour. The most visible aspect of this interaction is the existence of some kind of ‘locking’ phenomenon, where the inner vortex rings occupy the spaces left free between each pair of consecutive outer rings (or vice versa). One question arises from these observations: what is the impact of this inner/outer interaction in the evolution of the ‘shear-layer’ mode?

In order to answer this question one has to check out whether each (inner/outer) shear layer evolves according to the Kelvin–Helmholtz instability theory. In particular, the Strouhal numbers of the most amplified modes have to be the same values as predicted by the ‘linear stability theory’ for a mixing layer profile [27]. To analyse this we computed time spectra from the streamwise velocity signal at two locations. All spectra computed this way show peaks at a given Strouhal number. The results are listed in table 1.

Here we see that, whereas the outer shear layer instabilities agree very well with the expected value, the inner shear layers do not. A possible explanation for this fact can be gained by looking into the values of the actual frequencies. This is shown in table 2. This table shows that for DNS1 (no recirculation bubble), the inner and outer frequencies are exactly the same. This

Table 2. Frequencies f of the most amplified modes in the outer (o) and inner (i) shear layers for simulations DNS1 and DNS2. The frequencies are the same as displayed in table 1.

Simulation	f^o	f^i
DNS1	0.40	0.40
DNS2	0.45	0.30

suggests that the outer shear layer grows according to the theory (without ‘feeling’ the inner shear layer) and then imposes its evolution upon the inner shear layer.

The fact that the outer shear layer is dominating the inner layer can be explained in the following way. In DNS1 the initial vorticity of the outer shear layer is much larger than the inner one (see the initial inner and outer velocity ratios) which not only causes the outer vortex rings to appear sooner than the inner ones (see figure 9(a)), but also creates outer rings with total vorticity

$$\Omega_T^o(x) = \int_{R_m}^{\infty} |\vec{\Omega}(x, r)| dr, \quad (11)$$

which is higher than the total vorticity associated with the inner rings

$$\Omega_T^i(x) = \int_0^{R_m} |\vec{\Omega}(x, r)| dr, \quad (12)$$

$$\Omega_T^o(x) > \Omega_T^i(x). \quad (13)$$

This is likely to make the outer vortices dominant over the inner rings through inviscid vorticity induction (Biot–Savart), and therefore explains that the evolution of the inner structures is dictated by the motion of the outer, more important structures.

Things seem to be more complicated in DNS2. In this case also, the bigger intensity of the outer vortices, associated with the fact that the instability of the outer shear layer agrees with the theoretical value predicted by the Kelvin–Helmholtz instability (see table 1), makes one think that the same phenomenon might occur here. However, the existence of a back-flow region in this case greatly complicates the question. In this case the inner structures are not convected at the same speed as the outer ones, as can be assessed by the different values of their dimensional frequencies (see table 2). One possible explanation is that the back-flow region, being so close to the inner rings, will turn to decrease their travelling speed, thus making $f_*^i < f_*^o$ in this case. This phenomenon should be investigated with greater depth in future works.

To compare the evolution of the inner and outer shear layers, it is instructive to look into the downstream evolution of the following quantities:

$$E_r^i(x) = \sqrt{\frac{2\pi}{L_y L_z} \int_0^{R_m} \langle u_r'^2(x, r) \rangle r dr} \quad (14)$$

$$E_\theta^i(x) = \sqrt{\frac{2\pi}{L_y L_z} \int_0^{R_m} \langle u_\theta'^2(x, r) \rangle r dr} \quad (15)$$

$$E_r^o(x) = \sqrt{\frac{2\pi}{L_y L_z} \int_{R_m}^{\infty} \langle u_r'^2(x, r) \rangle r dr} \quad (16)$$

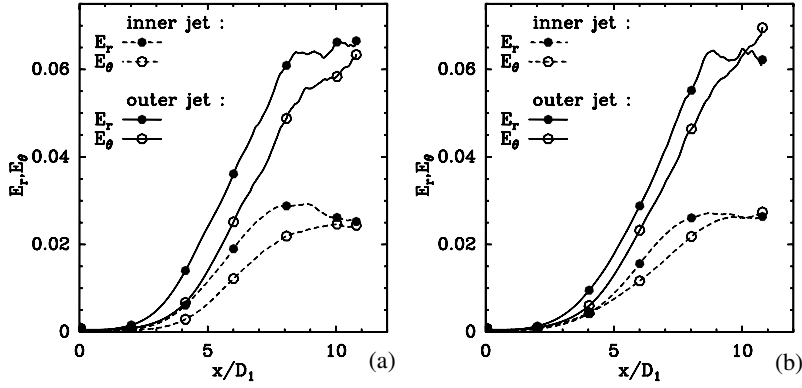


Figure 8. Downstream evolution of the radial, E_r (equations (14) and (16)) and tangential E_θ (equations (15) and (17)) contributions for the total kinetic energy in the inner (i) and outer (o) shear layers. (a) DNS1; (b) DNS2.

Table 3. Strouhal numbers of the most amplified modes at the end of the potential cores for DNS1 and DNS2, in the outer (o) and inner (i) shear layers. The Strouhal number is based on the inner and outer diameters, $Str_D^i = \frac{fD_1}{U_1}$ and $Str_D^o = \frac{fD_2}{U_2}$. The spectra were computed using time series of the streamwise velocity component located at $(r/D_1, x/D_1) = (0.75, 6)$ (outer layer) and $(r/D_1, x/D_1) = (0, 6)$ (inner layer).

Simulation	Str_D^o	Str_D^i
DNS1	0.40	0.60
DNS2	(5.0)	(5.0)

$$E_\theta^o(x) = \sqrt{\frac{2\pi}{L_y L_z} \int_{R_m}^{\infty} \langle u_\theta^2(x, r) \rangle r dr}. \quad (17)$$

In the above, $E_r(x)$ and $E_\theta(x)$, are the contributions of the radial and azimuthal Reynolds stresses to the turbulent kinetic energy at a given x location, respectively [28, 29]. The superscripts i and o define the inner and outer shear layers.

The downstream evolution of these quantities confirms the previous observations, showing that the outer instabilities begin to grow before the inner ones and dominate the whole transition region (i.e. $E_r^o(x) > E_r^i(x)$ and $E_\theta^o(x) > E_\theta^i(x)$) in DNS1 and DNS2 (figure 8).

4.2.2. Primary instabilities: jet preferred mode. In simple (non-coaxial) jets one often speaks of the so-called *preferred* jet mode which characterizes virtually all round jets, at sufficiently high Reynolds numbers. The frequency of the preferred jet mode is the frequency at which the vortex rings cross the end of the potential core and corresponds to a Strouhal number which is $0.24 < Str_D = fD/U_0 < 0.5$ [26]. It has been observed experimentally that coaxial jets also display this preferred jet frequency at the end of the central potential core [2]. Therefore, it is interesting to see whether the same happens in the present case. For this purpose table 3 shows the Strouhal numbers of the most unstable modes found at the end of the inner and outer potential cores for DNS1 and DNS2.

The table shows that for DNS1, the preferred mode is well recovered in the outer shear layer, but not in the inner layer. Since the preferred mode follows the evolution of the shear

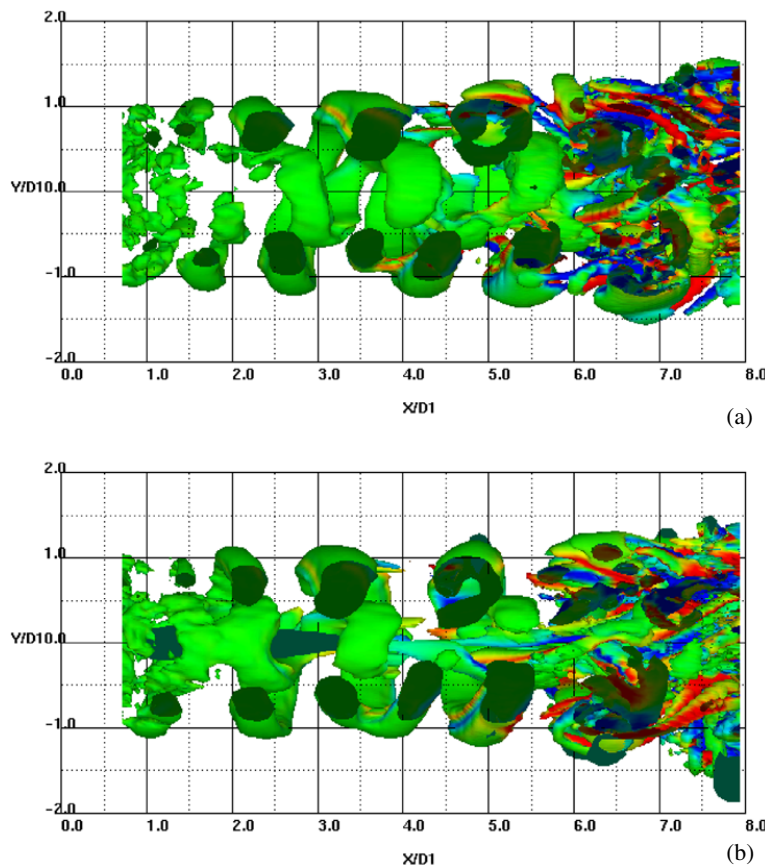


Figure 9. Cut view of positive Q isosurfaces coloured by the streamwise vorticity in DNS1 (a) and DNS2 (b).

layer mode, this fact can be explained as before: the outer vortex rings being more important; they evolve according to the theory and impose their evolution to the inner ones. As discussed before the same applies to the evolution of DNS2, although in this case the preferred mode is not well recovered. The value $Str_D^i = 5$ falls far outside the accepted range cited before. One way to explain this is through the quick convergence of the streamlines just after the recirculation bubble. The inner structures will have to cross, in that case, a much smaller section, which explains their acceleration (and higher passing frequency). Furthermore, these structures, being stretched in this way, will tend to increase their axial vorticity level, thus also increasing the level of small scale turbulence within themselves. It was observed, in agreement with this explanation, that in DNS2, unlike DNS1, the spectra show a range of high frequencies, rather than a given distinct peak (table 3 shows only the frequency corresponding to the highest energy). This point will be further discussed below.

The structure of the preferred mode can be studied in figure 9 showing isosurfaces of positive Q coloured by the streamwise vorticity for DNS1 and DNS2. Here we see that both the outer and inner vortices are organized into single helix shaped structures. The helices turn in the same sense due to the locking phenomenon described before. These observations raise one question: what is the most amplified mode in the present coaxial jets? To answer this question we recall the work of Cohen and Wygnanski [30], who made the connection between the form of the most

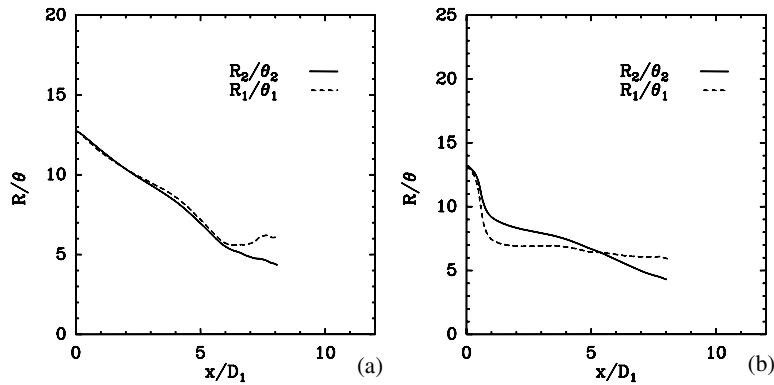


Figure 10. Downstream evolution of the ratio R/θ for the inner and outer jets ($R_1/\theta_1(x)$ and $R_2/\theta_2(x)$ where $\theta(x)$ is the local momentum thickness). (a) DNS1; (b) DNS2.

unstable wave and the resulting primary structures at the end of the potential core³. They showed that in single (non-coaxial) round jets the ratio R/θ dictates the most unstable mode as well as the resulting topology. For $R/\theta > 6.5$ the most unstable mode is axisymmetric $m = 0$ and axisymmetric structures are formed (vortex rings). For $R/\theta < 6.5$ the first non-symmetric mode ($m = 1$) has the highest amplification rate and leads to the formation of one helical structure. Although we have not computed the most unstable modes directly, we see that in DNS1 and DNS2 we have structures which correspond to the first helical mode ($m = 1$) (see figure 9). Moreover, figures 10(a) and (b) show that $R/\theta < 6.5$ for DNS1 and DNS2 at the end of the potential core. Therefore, it seems that the present results are consistent with the analysis from [30] and may indicate that their results are also valid for coaxial jets. Clearly, this point needs further investigation but the present results are encouraging. Note that the fact that R/θ is greater than 6.5 for most of the transition region ($x/D_1 < 4$) does not invalidate this result, as the helical arrangement found at the end of the potential core is likely to affect the flow upstream by a feed-back mechanism, thus selecting the first helical mode $m = 1$ as the most unstable, right from the inlet region.

4.2.3. Secondary instabilities. We have already seen the evolution of the primary structures in DNS1 and DNS2 which culminates in the formation of a single helix structure $m = 1$, made with the primary vortex rings. In the classical transition scenario for simple (non-coaxial) round jets, once the rings have been formed, one usually observes the emergence of a wavy structure along the azimuthal direction in each vortex ring. One usually speaks of azimuthal perturbations of mode n . Unlike the forced coaxial jets observed by da Silva and Métais [11], it is very difficult to discern an azimuthal perturbation in the rings from DNS1 and DNS2. Indeed, the primary rings show very little sign of any azimuthal perturbation in their shape. This agrees with what we can see in figures 8(a) and (b). In DNS1 and DNS2, $E_r(x)$, associated with the growth of the vortex rings, dominates $E_\theta(x)$, associated with the growth of the azimuthal perturbations $E_r(x) > E_\theta(x)$, until about $x/D_1 \approx 10$ where $E_r(x) \approx E_\theta(x)$. It seems that the growth of the vortex rings is dominating the evolution of the other instabilities until quite late in the transition process ($x/D_1 \approx 10$).

³ The most unstable wave is supposed to be of the form $p(x, r, \phi, t) = \tilde{p}(r) \exp[i(\alpha x + m\phi - \beta t)]$, where $i = \sqrt{-1}$ is the imaginary unit, β is the perturbation frequency, m the azimuthal wavenumber and $\alpha = \alpha_r + i\alpha_i$ a complex number in which α_r stands for the downstream wavenumber and α_i the rate of spatial amplification. If $m = 0$ the instability mode is axisymmetric (also called varicose mode); if $m \neq 0$ the wave has a helical shaped structure.

In DNS2 the presence of a back-flow region decreases the degree of domination of $E_r(x)$ over $E_\theta(x)$, i.e.

$$|E_r^i(x) - E_\theta^i(x)|_{DNS2} < |E_r^i(x) - E_\theta^i(x)|_{DNS1}, \quad (18)$$

and

$$|E_r^o(x) - E_\theta^o(x)|_{DNS2} < |E_r^o(x) - E_\theta^o(x)|_{DNS1}. \quad (19)$$

The recirculation bubble then acts as a ‘destabilizing’ effect in this predominance of the vortex rings in the transition mechanism.

Concerning the streamwise vortices, there is an interesting difference between DNS1 and DNS2. As discussed before, just after the back-flow region in DNS2 ($x/D_1 > 6.5$) the streamwise inner vortices not only appear much sooner than in DNS1, but are particularly elongated (figure 9(a)). Furthermore, these inner structures are characterized by extremely high values of vorticity reaching as high as twice the vorticity of the outer streamwise structures. It is possible to explain these observations by considering the production term in the axial vorticity equation

$$P_{(\Omega_x)} = \Omega_x \frac{\partial u_x}{\partial x} + \Omega_y \frac{\partial u_x}{\partial y} + \Omega_z \frac{\partial u_x}{\partial z}. \quad (20)$$

As in other flows with a recirculation bubble, there is a high streamwise velocity gradient $\partial u_x / \partial x$ in the region just after it. In the coaxial jet flow, this region is where the streamwise vortices begin to develop, and therefore contributes to create axial vorticity, Ω_x , by vortex stretching of the inner streamwise vortices, $\Omega_x \frac{\partial u_x}{\partial x}$. Thus, the back-flow region creates an additional source of axial vorticity production. A similar observation was made by da Silva and Métais [11] in a DNS of a forced coaxial jet with a back-flow region.

5. Conclusions

In the present work two DNSs (DNS1 and DNS2) were carried out in order to analyse the instabilities and transition in high velocity ratio coaxial jets ($r_u = 3.3$ and 23.5). In DNS1 two potential core regions form in the centre of the inner and outer jets, in agreement with the findings of Ko and Kwan [3] and Kwan and Ko [4]. For DNS2 ($r_u = 23.5$) the inner potential core does not exist due to the formation of a large recirculation region in $x/D_1 < 5$. In the present case the bubble encloses laminar flow and is in stationary motion, unlike the case of Rehab *et al* [2] who observed a similar structure undergoing solid body motion.

For both flows the Kelvin–Helmholtz instability in the inner and outer shear layers results in vortex rings which form, further downstream, an inner and outer helical structure. This corresponds to the development of a helical instability (mode $m = 1$) which agrees with the linear stability theory for a single jet, considering the ratio R/θ [30]. It was observed that the inner rings are ‘locked’ into the outer ones. Due to their higher vorticity, the latter impose their evolution upon the inner structures. It seems that the backflow region has only a minor influence on this process until the end of the potential core (for DNS2). The frequency of the preferred mode for single (non-coaxial) jets is well recovered in DNS1 ($r_u = 3.3$), but not in DNS2 ($r_u = 23.5$) due to the presence of the backflow region which greatly complicates the flow downstream. In this case it was observed that the secondary structures (pairs of streamwise vortices) have unusually high values of vorticity modulus. This can be explained by the recirculation bubble which stretches these structures, thus being an additional source of axial vorticity production.

Acknowledgment

The help of P Begou with the numerical-code parallelization is greatly acknowledged.

References

- [1] Dahm W J A, Friedler C E and Tryggvason G 1992 Vortex structure and dynamics in the near field of a coaxial jet *J. Fluid Mech.* **241** 371–402
- [2] Rehab H, Villiermaux E and Hopfinger E J 1997 Flow regimes of large-velocity-ratio coaxial jets *J. Fluid Mech.* **345** 357–81
- [3] Ko N W M and Kwan A S H 1976 The initial region of subsonic coaxial jets *J. Fluid Mech.* **73** 305–32
- [4] Kwan A S K and Ko N W M 1977 The initial region of subsonic coaxial jets. Part 2. *J. Fluid Mech.* **82** 237–87
- [5] Djeridane T 1994 Contribution à l'étude expérimentale de jets turbulents axisymétriques à densité variable *PhD Aix-Marseille II*
- [6] Ko N W M and Chan W T 1979 The inner regions of annular jets *J. Fluid Mech.* **93** 549–84
- [7] Rehab H 1997 Structure de l'écoulement et mélange dans le champ proche des jets coaxiaux *PhD Grenoble*
- [8] Akselvoll K and Moin P 1996 Large-eddy simulation of turbulent confined coannular jets *J. Fluid Mech.* **315** 387–411
- [9] Salvetti M V 1996 Numerical simulations of transitional axisymmetric coaxial jets *AIAA J.* **34** 736–43
- [10] Salvetti M V 2000 Effects of the velocity ratio on vorticity dynamics and mixing in coaxial jet flows *1st Turbulent Shear Flow Phenomena*
- [11] da Silva C B and Métais O 2001 Coherent structures in excited spatially evolving round jets *Direct and Large-Eddy Simulation* vol 4 (New York: Kluwer)
- [12] Lele S K 1992 Compact finite difference schemes with spectral-like resolution *J. Comput. Phys.* **103** 15–42
- [13] Canuto C, Hussain M Y, Quarteroni A and Zang T A 1987 *Spectral Methods in Fluid Dynamics* (New York: Springer)
- [14] Le H and Moin P 1991 An improvement of fractional-step methods for the incompressible Navier–Stokes equations *J. Comput. Phys.* **92** 369–79
- [15] Williamson J H 1980 Low-storage Runge–Kutta schemes *J. Comput. Phys.* **35** 48–56
- [16] Orlansky I 1976 A simple boundary condition for unbounded hyperbolic flows *J. Comput. Phys.* **21** 251–69
- [17] Gonze M A 1993 Simulation numérique des sillages en transition à la turbulence *PhD Grenoble*
- [18] da Silva C B and Métais O 2002 Vortex control of bifurcating jets: a numerical study *Phys. Fluids* **14** 3798–819
- [19] da Silva C B and Métais O 2002 On the influence of coherent structures upon interscale interactions in turbulent plane jets *J. Fluid Mech.* **473** 103–45
- [20] da Silva C B 2001 The role of coherent structures in the control and interscale interactions of round, plane and coaxial jets *PhD Grenoble*
- [21] Comte P, Silvestrini J and Begou P 1998 Streamwise vortices in the large-eddy simulations of mixing layers *J. Mech. B/Fluids* **17** 4:615–37
- [22] Hunt J C R, Wray A A and Moin P 1988 Eddies, stream, and convergence zones in turbulent flows *Annual Research Briefs* Center for Turbulence Research, Stanford University, Stanford
- [23] Dubief I and Delcayre F 2000 On coherent-vortex identification in turbulence *J. Turbulence* **1** 011
- [24] Zaman K B M Q and Hussain K M F 1980 Vortex pairing in a circular jet under controlled excitation. Part 1. General jet response *J. Fluid Mech.* **101** 449–91
- [25] Crow S C and Champagne F H 1971 Orderly structure in jet turbulence *J. Fluid Mech.* **48** 547–91
- [26] Gutmark E and Ho C-M 1983 Preferred modes and the spreading rates of jets *Phys. Fluids A* **26** 2932–8
- [27] Michalke A and Hermann G 1982 On the inviscid instability of a circular jet with external flow *J. Fluid Mech.* **114** 343–59
- [28] Danaila I, Dusek J and Anselmet F 1997 Coherent structures in a round, spatially evolving, unforced, homogeneous jet at low Reynolds numbers *Phys. Fluids* **9** 3323–42
- [29] Brancher P, Chomaz J M and Huerre P 1993 Direct numerical simulations of round jets: vortex induction and side jets *Phys. Fluids* **6** 1768–74
- [30] Cohen J and Wygnanski I 1987 The evolution of instabilities in the axisymmetric jet. Part 1. The linear growth of the disturbances near the nozzle *J. Fluid Mech.* **176** 191–219